

DYNAMO EFFECTS IN MAGNETOROTATIONAL TURBULENCE WITH FINITE THERMAL DIFFUSIVITY

OLIVER GRESSEL

NORDITA, KTH Royal Institute of Technology and Stockholm University, Roslagstullsbacken 23, 106 91 Stockholm, Sweden

Draft version April 10, 2013

ABSTRACT

We investigate the saturation level of hydromagnetic turbulence driven by the magnetorotational instability in the case of vanishing net flux. Motivated by a recent paper of Bodo, Cattaneo, Mignone, & Rossi, we here focus on the case of a non-isothermal equation of state with constant thermal diffusivity. The central aim of the paper is to complement the previous result with closure parameters for mean-field dynamo models, and to test the hypothesis that the dynamo is affected by the mode of heat transport. We perform computer simulations of local shearing-box models of stratified accretion disks with approximate treatment of radiative heat transport, which is modeled via thermal conduction. We study the effect of varying the (constant) thermal diffusivity, and apply different vertical boundary conditions. In the case of impenetrable vertical boundaries, we confirm the transition from mainly conductive to mainly convective vertical heat transport below a critical thermal diffusivity. This transition is however much less dramatic when more natural outflow boundary conditions are applied. Similarly, the enhancement of magnetic activity in this case is less pronounced. Nevertheless, heating via turbulent dissipation determines the thermodynamic structure of accretion disks, and clearly affects the properties of the related dynamo. This effect may however have been overestimated in previous work, and a careful study of the role played by boundaries will be required.

Subject headings: accretion, accretion disks – dynamo – magnetohydrodynamics (MHD) – turbulence

1. INTRODUCTION

There are few concepts in classical physics that are equally fundamental as the conservation of angular momentum. One formidable consequence of this law is the formation of gaseous accretion disks around a wide range of astrophysical objects. Yet to explain observed luminosities based on the release of gravitational binding energy (King et al. 2007), a robust mechanism is required to circumvent the consequences of angular momentum conservation. Being sufficiently ionised, these discs harbor dynamically important magnetic fields, which render the disk unstable to a mechanism called magnetorotational instability (MRI, Balbus & Hawley 1998), releasing energy from the differential rotation and converting it into turbulent motions. Ultimately, these motions are what is powering the redistribution of angular momentum on large scales. In the absence of externally imposed large-scale fields, a separate dynamo mechanism may be required to replenish sufficiently coherent fields to drive sustained MRI turbulence (Vishniac 2009). This requirement becomes particularly apparent in models that neglect the vertical structure of the disk. In this case a convergence problem has been encountered (Pessah et al. 2007; Fromang & Papaloizou 2007; Bodo et al. 2011), which has been attributed to the lack of an outer scale of the turbulence (Davis et al. 2010). An alternative explanation has been suggested by Kitchatinov & Rüdiger (2010), who point out the problem of resolving the radial fine-structure related to non-axisymmetric MRI modes (required to circumvent Cowling’s “no dynamo” theorem). Convergence can naturally be recovered when accounting for the vertical stratification of the disk (Shi et al. 2010; Oishi & Mac Low 2011). Together with rotational anisotropy, the introduced vertical inhomogeneity can produce a pseudo-scalar leading to a classical mean-field dynamo (Brandenburg et al. 1995a). In a previous

paper (Gressel 2010, hereafter G10), we have inferred mean-field closure parameters from isothermal stratified MRI simulations (also see Brandenburg 2008) and demonstrated that the “butterfly” pattern (see e.g. Miller & Stone 2000; Shi et al. 2010; Simon et al. 2012) typical for stratified MRI can in fact be described in such a framework. In the current paper, we aim to extend this line of work towards a more realistic thermodynamic treatment, including heating from turbulent dissipation (Gardiner & Stone 2005; Piontek et al. 2009) and crude heat transport. This new effort is largely initiated by a recent paper of Bodo, Cattaneo, Mignone, & Rossi (2012), hereafter BCMR. The authors make the intriguing suggestion that the treatment of the disk thermodynamics will have a strong effect on the dynamo and accordingly on the saturation level of the turbulence. This is in contrast to the result of Brandenburg et al. (1995b), who find that turbulent transport is not affected by the presence of convection.

As a first step to improve the realism of MRI simulations compared to the commonly applied isothermal equation of state, BCMR assume thermal conduction with constant thermal diffusivity, κ . They then identify a critical value κ_c below which the primary mode of vertical heat transport changes from being predominantly conductive to being dominated by turbulent convective motions. One motivation of the present work is to scrutinize these models and at the same time obtain mean-field closure coefficients for the two suggested regimes, thereby confirming the assumption that the thermodynamic treatment of the disk affects underlying dynamo processes. A second focus of our paper will be the authors’ choice of impenetrable vertical boundary conditions, which we find to have profound implications for the resulting vertical disk equilibrium.

2. MODEL AND EQUATIONS

The simulations presented in this paper extend the simulation of Gressel (2010) to include a more realistic treat-

ment of thermodynamic processes as pioneered by Bodo et al. (2012). Simulations are carried out using the second-order accurate NIRVANA-III code (Ziegler 2004), which has been supplemented with the HLLD Riemann solver (Miyoshi & Kusano 2005) for improved accuracy. We solve the standard MHD equations in the shearing-box approximation (Gressel & Ziegler 2007) employing the finite-volume implementation of the orbital advection scheme as described in Stone & Gardiner (2010); for interpolation we use the Fourier method by Johansen et al. (2009). We here neglect explicit viscous or resistive dissipation terms but include an artificial mass diffusion term (as described in Gressel et al. 2011) to circumvent time-step constraints due to low density regions in upper disk layers. We remark that, owing to the total-variation-diminishing (TVD) nature of our numerical scheme and the total energy formulation, heating via dissipation of kinetic and magnetic energy at small scales is accounted for even in the absence of explicit (or artificial) dissipation terms.

Written in a Cartesian coordinate system $(\hat{x}, \hat{y}, \hat{z})$ and with respect to conserved variables ρ , $\rho\mathbf{v}$, and the total energy $e = \epsilon + \frac{1}{2}\rho\mathbf{v}^2 + \frac{1}{2}\mathbf{B}^2$, with ϵ being the thermal energy density, the equations read:

$$\partial_t \rho + \nabla \cdot (\rho \mathbf{v}) = 0, \quad (1)$$

$$\partial_t (\rho \mathbf{v}) + \nabla \cdot [\rho \mathbf{v} \mathbf{v} + p^* \mathbf{I} - \mathbf{B} \mathbf{B}] = \rho [-\nabla \Phi + \mathbf{a}_i], \quad (2)$$

$$\partial_t e + \nabla \cdot [(e + p^*) \mathbf{v} - (\mathbf{v} \cdot \mathbf{B}) \mathbf{B}] = \rho \mathbf{v} \cdot [-\nabla \Phi + \mathbf{a}_i] + \nabla \cdot (k \nabla T), \quad (3)$$

$$\begin{aligned} \partial_t \mathbf{B} - \nabla \times (\mathbf{v} \times \mathbf{B}) &= 0, \\ \nabla \cdot \mathbf{B} &= 0, \end{aligned} \quad (4)$$

with the total pressure given by $p^* \equiv p + \frac{1}{2}\mathbf{B}^2$, and a fixed external potential $\Phi(z) = \frac{1}{2}\Omega^2 z^2$. The inertial acceleration $\mathbf{a}_i \equiv 2\Omega (q\Omega x \hat{x} - \hat{z} \times \mathbf{v})$ arises due to tidal and Coriolis forces in the local Hill system, rotating with a fixed $\Omega \equiv \Omega_0 \hat{z}$, and where the shear-rate $q \equiv d \ln \Omega / d \ln R$ has a value of $-3/2$ for Keplerian rotation.

We furthermore assume an adiabatic equation of state, such that the gas pressure relates to the thermal energy density as $p = (\gamma - 1)\epsilon$, with the ratio of specific heats $\gamma = \frac{5}{3}$, as appropriate for a mono-atomic dilute gas.

Finally, the temperature, T , appearing in the conductive energy flux, is obtained via the ideal-gas law $p = \rho T$, where we chose units such that the factor $\bar{\mu} m_H / k_B$ relating to the gas constant disappears. Following the approach taken by BCMR, we adopt a thermal conductivity, k , in terms of a constant diffusivity coefficient κ , related via

$$k = \frac{\gamma}{\gamma - 1} \rho \kappa. \quad (5)$$

For the isothermal run, we do not evolve Equation (3) but instead obtain the gas pressure via $p = \rho T_0$, with fixed temperature $T_0 = 1$. Note that, in our units, T_0 differs from BCMR by a factor of two, owing the alternative definition of the initial hydrostatic equilibrium, which is

$$\rho(z) = \rho_0 e^{-z^2/2H^2} = \rho_0 e^{-\Omega^2 z^2/T_0} \quad (6)$$

in our case. For all simulations, we adopt the same box size of $H \times \pi H \times 6H$ at a numerical resolution of $32 \times 96 \times 192$ grid cells in the radial, azimuthal, and vertical direction, respectively. This corresponds to a linear resolution of $\sim 32/H$ in all three space dimensions.

TABLE 1
OVERVIEW OF SIMULATION PARAMETERS, AND RESULTS.

	EoS	$\kappa [H^2\Omega]$	vBC	$\langle \overline{M_{xy}} \rangle [10^{-2}p_0]$	$T_{\text{mid}} [T_0]$
M1	isoth.	–	outfl.	0.54 ± 0.14	–
M2	adiab.	0.120	outfl.	0.63 ± 0.17	1.23
M3	adiab.	0.004	outfl.	0.81 ± 0.21	1.74
M4	adiab.	0.004	wall	1.53 ± 0.34	4.94

As typical for shearing box simulations, we initialize the velocity field with the equilibrium solution $\mathbf{v} = q\Omega x \hat{y}$, and adiabatically perturb the density and pressure by a white-noise of 1% rms amplitude. The magnetic configuration is of the zero-net-flux (ZNF) type with a basic radial variation

$$\mathbf{B} = B_0 \sin(2\pi x/L_x) \hat{z}. \quad (7)$$

To obtain a uniform transition into turbulence, we further scale the vertical field with a factor $(p(z)/p(0))^{1/2}$ resulting in $\bar{\beta}_P = \text{const}$ ($= 1600$ initially).¹ Owing to the divergence constrain, this of course can only be done by introducing a corresponding radial field at the same time. In practice, we specify a suitable vector potential.

Horizontal boundary conditions (BCs) are of the standard sheared-periodic type, and we correct the hydrodynamic fluxes to retain the conservation properties of the finite-volume scheme (Gressel & Ziegler 2007). For the vertical boundaries, we implement stress-free BCs (i.e., $\partial_z v_x = \partial_z v_y = 0$) with two different cases for the treatment of the vertical velocity component v_z , namely: (i) impenetrable, and (ii) allowing for outflow (but preventing in-fall of material from outside the domain). We will demonstrate that this distinction will have profound implications for the resulting density and temperature profiles within the box. To counter-act the severe mass loss occurring in the case of open BCs, we continuously rescale the mass density, keeping the velocity and thermal energy density intact.² Unlike in earlier work (Gressel et al. 2012), which was adopting an isothermal equation of state, we here do not restore towards the initial profile, but simply rescale the current profile. This is, of course, essential to allow for an evolution of the vertical disc structure, owing to heating via turbulent dissipation. We remark that such a replenishing of material can be thought of as a natural consequence of radial mass transport within a global disk.

As in BCMR, we use $\partial_z B = 0$, $B_x = B_y = 0$ as boundary condition for the magnetic field, and impose a constant temperature $T = T_0$ at the top and bottom surfaces of the disk. The latter choice is motivated by the assumption that the upper disk layers are likely optically thin, and there exists a thermal equilibrium with their surroundings. As in previous work, we compute the density and thermal energy of the adjacent grid cells in the z direction to be in hydrostatic equilibrium.

3. RESULTS

The main motivation of this paper is to reproduce, as closely as possible, the results of BCMR, where we then aim to establish mean-field dynamo effects for the contrasting cases of efficient versus inefficient thermal conduction, as studied there. Moreover, we shall begin to explore the impact of vertical

¹ Here and in the following, over-bars denote horizontal averaging. Additional averaging in time is denoted by angle brackets, $\langle \rangle$.

² Technically, this amounts to a volumetric cooling of the disk.

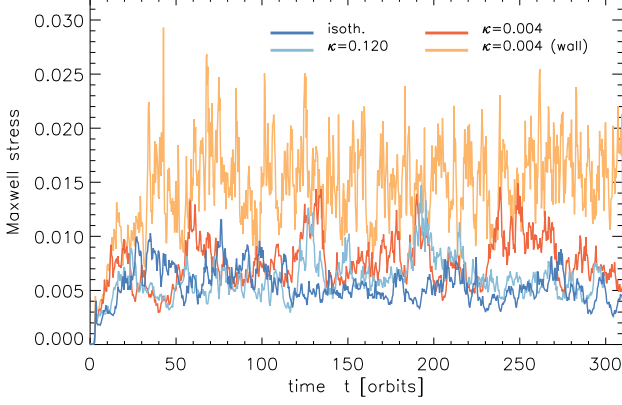


FIG. 1.— Time evolution of the volume-averaged Maxwell stress for the different models. For reference, we also list time averages in Table 1.

boundary conditions, by studying the somewhat more realistic case allowing for a vertical outflow of material.

We have performed in total four simulations: the two main simulations (‘M2’ and ‘M3’) adopt thermal diffusivity of $\kappa = 0.12$, and $\kappa = 0.004$, respectively, representing the regimes of efficient and inefficient thermal transport (at molecular level), respectively. For both these simulations, and for a third isothermal reference run (model ‘M1’), we adopt *outflow* boundary conditions. To assess the impact of the imposed vertical BCs (see column “vBC” in Table 1), and to make direct contact with previous work, we adopt a fourth model, ‘M4’, with a value $\kappa = 0.004$, and *impenetrable* boundaries at the top and bottom of the domain (labeled “wall” in the following).

3.1. Comparison with BCMR

We ran the different models for approximately 300 orbital times, $2\pi\Omega^{-1}$; note that BCMR use time units of Ω^{-1} instead. All time averages are taken in the interval $t = [50, 300]$. For the isothermal reference run, we obtain a time-averaged Maxwell stress,

$$\langle \overline{M}_{xy} \rangle \equiv - \langle (B_x - \overline{B}_x) (B_y - \overline{B}_y) \rangle, \quad (8)$$

of $(0.54 \pm 0.14) \times 10^{-2}$, which is comparable to the $\kappa = 0.12$ case with $(0.63 \pm 0.17) \times 10^{-2}$. In the case $\kappa = 0.04$ with outflow boundaries we find a somewhat higher value of $(0.81 \pm 0.21) \times 10^{-2}$, which is however significantly lower than in the otherwise identical case with impenetrable boundaries with $(1.53 \pm 0.34) \times 10^{-2}$. While stresses are indeed increased (by approximately 30%) at lower conductivity, clearly, the effect of the treatment of the boundaries is much more significant.

Due to the strong fluctuations, the relative amplitudes are best seen in Figure 2, where we plot time-averaged vertical profiles of \overline{M}_{xy} normalized to the initial midplane gas pressure, p_0 . Compared to the isothermal case M1, the thermally conductive model M2 has a very similar vertical structure. The low conductivity model M3, where turbulent overturning motions dominate, is not too different in terms of its vertical profile either. Markedly, model M4, with impenetrable vertical BCs, shows maxima of \overline{M}_{xy} around $|z| = 1.5 H$. This is similar to the profiles shown in figure 8 of BCMR, but note that their model shows a strong peak within $0.5 H$ of the vertical boundaries, while we only observe a very thin boundary layer in our model.

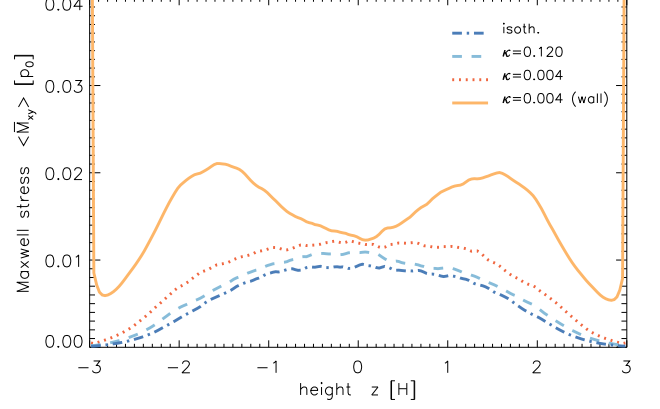


FIG. 2.— Time-averaged (for $t \in [50, 300]$ orbits) vertical profiles of the average Maxwell stress for the different models.

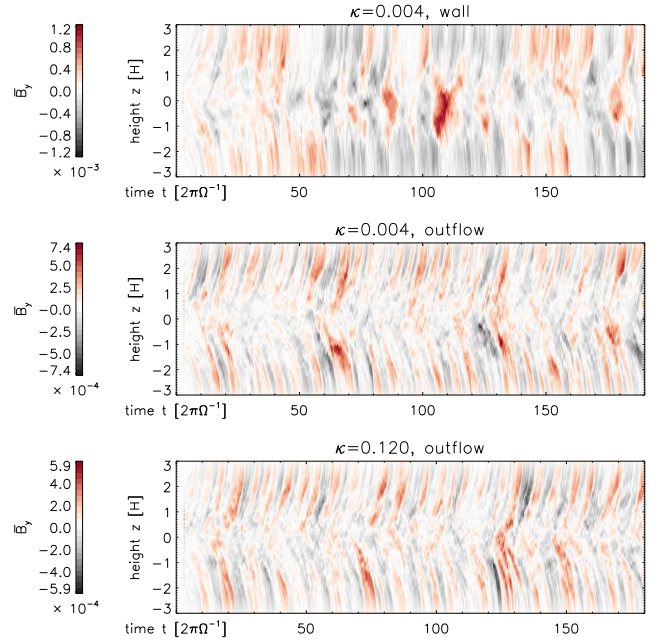


FIG. 3.— Space-time “butterfly” diagrams of the azimuthal magnetic field \overline{B}_y for: model M4 with $\kappa = 0.004$ and impenetrable boundaries (top), model M3 with $\kappa = 0.004$ and outflow boundaries (middle), and model M2 with $\kappa = 0.12$ and outflow (lower panel).

At the end of their result section, BCMR point-out that the spatio-temporal behavior of the dynamo is remarkably different between the $\kappa = 0.12$, and $\kappa = 0.004$ cases (see their figure 9). If we compare to run M4 with impenetrable boundaries (uppermost panel of Figure 3), we indeed find a similarly irregular butterfly diagram. BCMR argue that they find “no evidence for cyclic activity or pattern propagation” in the conductive regime. In contrast to this, looking at Figure 3, it appears that even model M4 at some level shows a propagating dynamo wave. More importantly, models M2, and M3 (which presumably are in the conductive, and convective regimes, respectively) show extremely similar dynamo patterns and cycle frequency (middle and lower panels in Figure 3). This again suggests that the vertical boundaries have a profound effect on the mechanism of vertical heat transport and, as a consequence, on the dynamo.

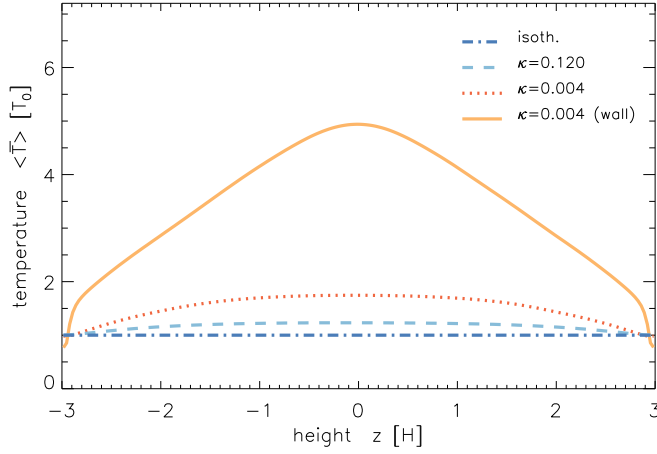


FIG. 4.— Time-averaged (for $t \in [50, 300]$ orbits) temperature profiles.

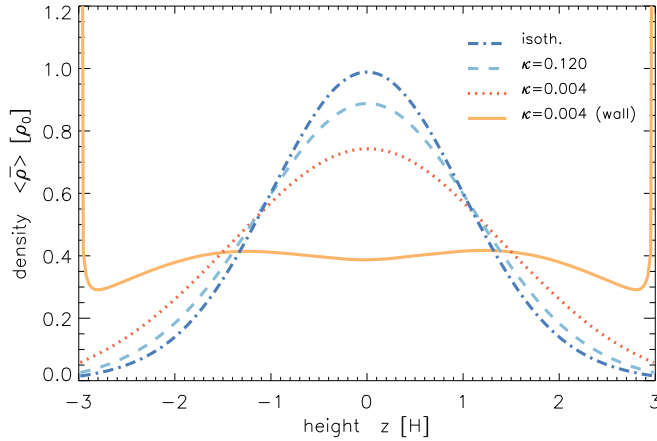


FIG. 5.— Same as Figure 4, but for the average density.

To establish the fact that our model M4 is indeed comparable to the corresponding simulation of BCMR, we now look at vertical profiles of the gas density and temperature. For the latter, BCMR had found a peculiar “tent” shape (see their figure 4), i.e. a linear dependence of \bar{T} on z , joined together at $z = 0$ by a parabolic segment. In Figure 4, we compile the $\bar{T}(z)$ profiles, and such a tent-like profile can indeed be seen for model M4. However, in the case of low thermal diffusivity, $\kappa = 0.004$, we observe a much weaker deviation from the isothermal profile with outflow boundary conditions.

Along with the tent-shaped temperature profile, BCMR found that heat transport from convection would erase the vertical density stratification and lead to a constant density near the disk midplane (see their figure 5). We observe a very similar density profile for model M4, which moreover shows strong density peaks at the domain boundary. These peaks are a consequence of enforcing the hydrodynamic fluxes to be zero at the domain boundaries. Unlike for impenetrable vertical boundaries, model M3 shows a more regular Gaussian density profile. For models M1-M3, the width of the bell-shaped density profiles is consistent with the trend in temperature and reflects hydrostatic equilibrium. Apparently, such an equilibrium cannot be obtained if solid-wall boundaries are applied.

BCMR conjecture that when κ crosses a critical value of $\kappa_c \simeq 0.02$, the vertical heat transport changes from being mainly conductive to being predominantly convective. This

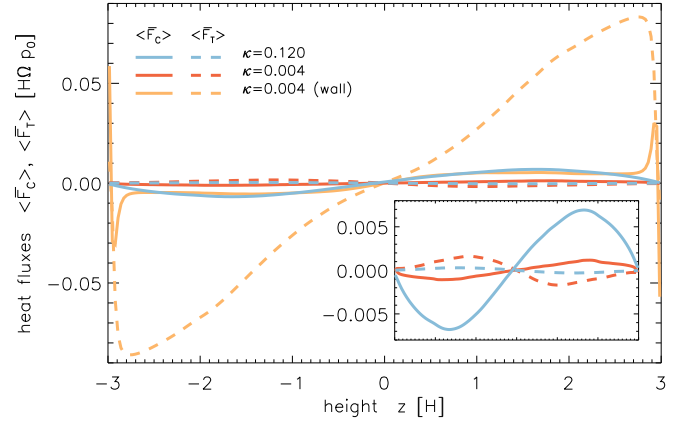


FIG. 6.— Conductive heat flux $\langle \bar{F}_C \rangle$ (solid lines), and turbulent convective heat flux $\langle \bar{F}_T \rangle$ (dashed lines) for the three non-isothermal models.

was illustrated by their figure 6, where they compared the conductive heat flux

$$\bar{F}_C = -\frac{\gamma}{\gamma-1} \kappa \bar{\rho} \frac{d\bar{T}}{dz}, \quad (9)$$

with the mean turbulent heat flux

$$\bar{F}_T = \frac{\gamma}{\gamma-1} \overline{\rho v_z (T - \bar{T})}, \quad (10)$$

where horizontal lines as usual indicate averages over the x and y directions. In Figure 6, we show the corresponding quantities for our non-isothermal runs: as in previous plots, model M4 agrees very well with the result of BCMR, but again differs significantly from the otherwise identical model M3 with outflow boundary conditions. Compared to M4, the net transport of heat is much reduced in the case of models M2, and M3. For clarity we plot these curves separately in the inset of Figure 6 with magnified ordinate. Much as expected, model M2 is dominated by a positive (i.e. outward) conductive heat flux, whereas the turbulent flux is negligible. Unlike model M4 with solid-wall boundaries, the low-conductivity model, M3, only shows a very moderate level of convective heat flux, and notably one of the opposite sign. This negative flux appears to largely balance its positive conductive counterpart, implying low levels of net-conductive heat transport towards the disk surface and net-convective transport towards the midplane. It is instructive to note that the heating predominantly occurs at $z \simeq \pm 2 H$, where the velocity and magnetic field fluctuations are highest, and not, as one might think, near the midplane.

3.2. Mean-field coefficients

One objective of this work was to test the dependence of the dynamo on the mechanism of vertical heat transport. One way of doing this is to establish mean-field closure parameters for the new class of models with constant thermal diffusivity. Like in previous work, we utilize the test-field (TF) method (Schrinner et al. 2005, 2007) to measure coefficients such as the α effect, turbulent pumping, and eddy diffusivity. The used method (Brandenburg 2005) is “quasi-kinematic” (Rheinhardt & Brandenburg 2010) in the sense that it has been found to remain valid into the non-kinematic regime in the absence of magnetic background fluctuations (Brandenburg et al. 2008) – whether this covers MRI is a topic of discussion. We here only briefly recapitulate the general

framework of mean-field MHD and refer the reader to G10 for a more detailed description. A recent review about mean-field dynamos can be found in Brandenburg et al. (2012).

For the shearing-box approximation, due to its periodic character in the horizontal direction, there are no characteristic gradients expected in the radial or azimuthal directions. The natural mean-fields are accordingly those, which only vary in the vertical direction. With respect to the velocity $\mathbf{u} = \mathbf{v} - q\Omega x \hat{\mathbf{y}}$, the mean-field induction equation reads

$$\partial_t \bar{\mathbf{B}}(z) = \nabla \times [\bar{\mathbf{u}}(z) \times \bar{\mathbf{B}}(z) + \mathcal{E}(z) + (q\Omega x \hat{\mathbf{y}}) \times \bar{\mathbf{B}}(z)], \quad (11)$$

where we have ignored a contribution due to microscopic magnetic diffusivity. Note that the explicit x dependence in the shear term, $q\Omega x \hat{\mathbf{y}}$, drops out once the curl operation is applied. Furthermore, $\bar{B}_z = \bar{B}_z(t=0) = 0$ because of flux conservation in the periodic box. In this description, turbulence effects due to *correlated* velocity and magnetic field fluctuations are embodied in the mean electromotive force

$$\mathcal{E}(z) \equiv \overline{\mathbf{u}' \times \mathbf{B}'}, \quad (12)$$

which is typically parametrized as (Brandenburg 2005):

$$\mathcal{E}_i(z) = \alpha_{ij}(z) \bar{B}_j(z) - \tilde{\eta}_{ij}(z) \varepsilon_{jkl} \partial_k \bar{B}_l(z), \quad (13)$$

where $i, j \in \{x, y\}$, $k = z$.

Given explicit knowledge of the rank-two α and $\tilde{\eta}$ tensors, this closure allows to formulate the mean-field induction equation (11) in terms of mean quantities alone, leading to the classical $\alpha\Omega$ dynamo description, first applied to MRI turbulence by Brandenburg et al. (1995a).

Tensor coefficients representing the closure parameters are presented in Figure 7 for model M2, with a high value $\kappa = 0.12$ of the thermal diffusivity. The obtained profiles are largely similar to the corresponding curves of the isothermal model M1 (not shown), which moreover agree³ with previous isothermal results reported in G10. Notably, for model M2, the contrast between the disc midplane and the upper disc layers is somewhat less pronounced compared to the purely isothermal case. This trend is continued when going to lower thermal diffusivity (see Figure 8 below). Unlike reported in G10, we now find α_{xx} and α_{yy} to be predominantly of the *same* sign, which would argue in favor of a kinematic (rather than magnetic) origin of the effect. Note however the significant fluctuations in α_{xx} , which cast some doubt on whether this coefficient can be meaningfully determined in the presence of shear. On the other hand, a fluctuating α should not be disregarded as a possible source of a mean-field dynamo (Vishniac & Brandenburg 1997).

Before we proceed, we briefly discuss the remaining coefficients. In panel (b) of Figure 7, we show the off-diagonal tensor elements of the α tensor, which are dominantly symmetric, i.e. $\alpha_{xy} \simeq \alpha_{yx}$. We remark that for the classical diamagnetic pumping effect, one would require *anti*-symmetric parity. The observed symmetry may however be interpreted as differential pumping, i.e. transporting radial and azimuthal field in opposite directions. For reference, we plot the mean vertical velocity \bar{u}_z (see dashed line), which additionally transports the mean field and hence leads to the

³ This is with the exception of α_{xx} , which generally appears to be poorly constrained by our simulations.

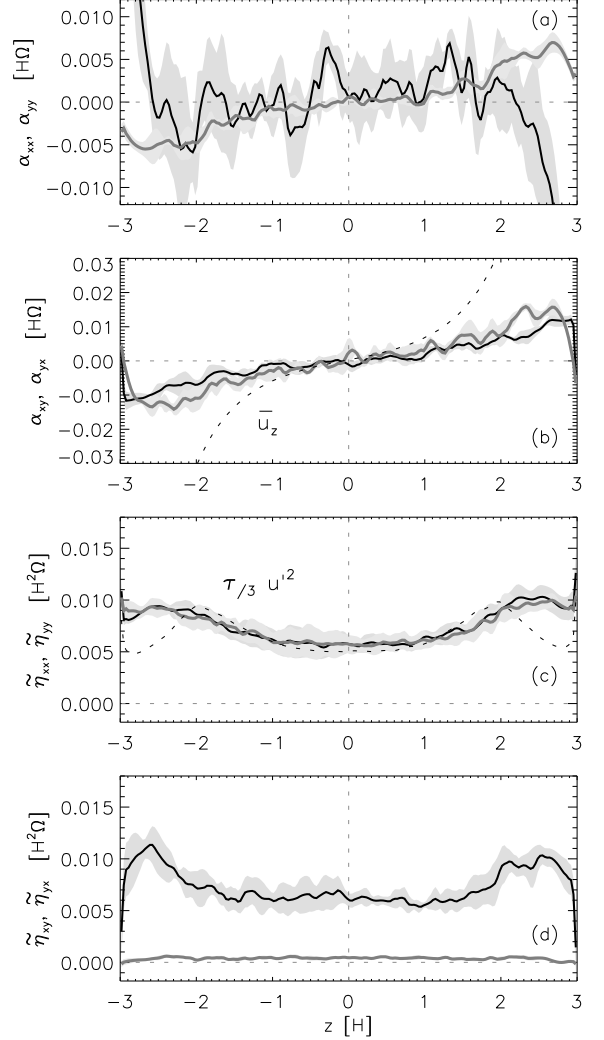


FIG. 7.— Mean-field coefficients computed via the TF method for model M2 with $\kappa = 0.120$. Axis labels indicate curves plotted in dark (α_{xx}, \dots) or light (α_{yy}, \dots) colours, respectively. The mean vertical velocity, \bar{u}_z , in panel (b), and the classical estimate for the turbulent diffusion, in panel (c), are shown as dashed lines.

characteristic acceleration in the butterfly diagram. The diagonal parts of the $\tilde{\eta}$ tensor are shown in panel (c), where we also plot the rms velocity fluctuation (dashed line). Apart from the boundary layers, the turbulent diffusivity agrees well with the theoretical expectation

$$\eta_T \simeq \frac{\tau}{3} u'^2, \quad (14)$$

that is, assuming a coherence time $\tau = 0.03 \Omega^{-1}$ of the turbulence. Given the dominance of the azimuthal field, the coefficients $\tilde{\eta}_{xx}$ and $\tilde{\eta}_{yy}$ are surprisingly isotropic (unlike predicted by Vainshtein, Parker, & Rosner 1993). It is however interesting to note that while $\tilde{\eta}_{xy}$, shown in panel (d) of Figure 7, is identical to the diagonal elements of the diffusivity tensor in panel (c), its counterpart $\tilde{\eta}_{yx}$ is much smaller. With negative shear and both coefficients positive, the dynamo based on the Rädler (1969) effect is decaying (cf. the dispersion relation in Brandenburg 2005, appendix B). This does however not exclude the possibility that $\tilde{\eta}_{yx}$ has an effect on the overall pattern propagation.

We now proceed to the corresponding coefficients for the

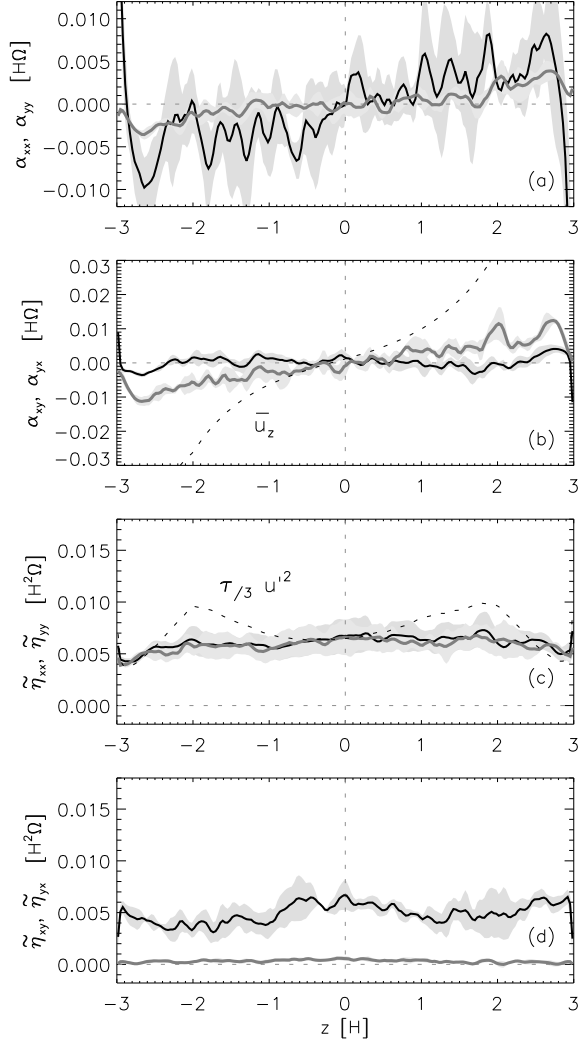


FIG. 8.— Same as Figure 7, but for the model M3 with $\kappa = 0.004$. Note that for the sake of direct comparison, axis ranges are kept fixed with respect to the previous figure.

case of inefficient thermal conduction. In Figure 8 we accordingly show the α and $\tilde{\eta}$ tensor components for model M3. We recall that in the quasi-isothermal case (cf. Figure 7) the α_{xx} and α_{yy} coefficients showed a trend to flatten and even reverse their slope near the midplane (also cf. figure 9 in Brandenburg 2008). This was reasoned to be related to a *negative* α effect due to magnetic buoyancy (Brandenburg 1998; Rüdiger & Pipin 2000). In contrast, here the α_{xx} curve shows a more monotonic dependence on z , indicating that such magnetic effects may be less pronounced in this case. Such a trend appears consistent with reduced magnetic buoyancy in the case of a stiffer effective equation of state. Moving on to panel (b), we note that α_{xy} is now suppressed and even shows a slight trend to change its sign – indicating a possible significance of diamagnetic pumping in the adiabatic case. For the turbulent diffusivity plotted in panel (c), we observe a significant deviation from the classical expectation (dashed line), resulting in a nearly constant $\eta_T(z)$. We conclude that the equation of state and the means by which energy is transported to the upper disk layers indeed have subtle effects on the inferred dynamo tensors. Which of the differences seen between Figures 7 and 8 is in the end responsible for the enhanced dy-

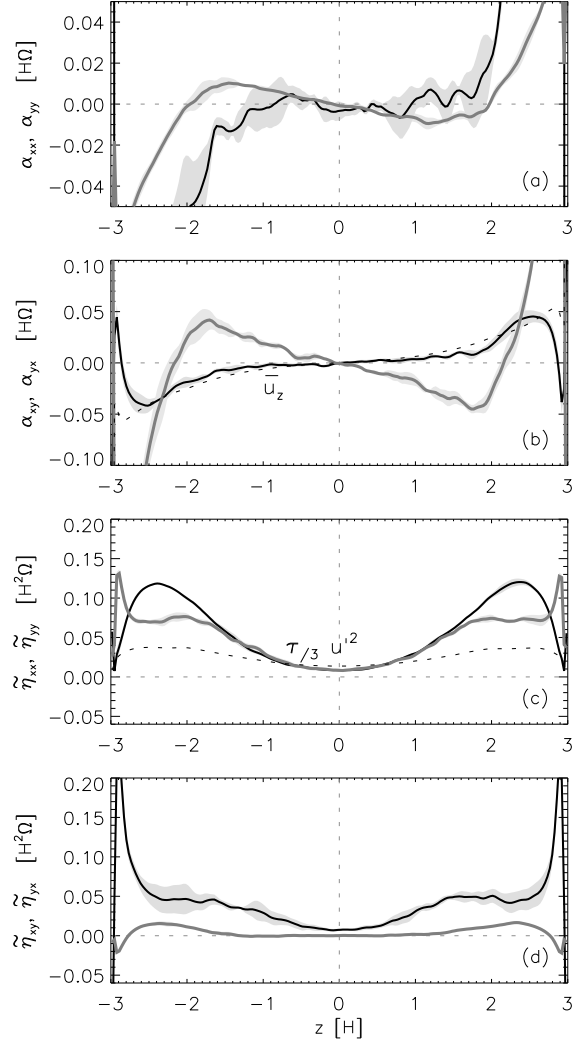


FIG. 9.— Same as Figure 7, but for the model M4 with $\kappa = 0.004$ and impenetrable vertical boundaries. Note the different axis ranges as compared to the previous two figures.

namo activity seen in model M3, will require further careful study. For completeness, in Figure 9, we also show the results for model M4, where dynamo coefficients are larger by a factor of several. This can be considered consistent with the much higher Maxwell stresses observed in this case. Unlike for model M3, $\tilde{\eta}(z)$ now shows a pronounced z dependence, and α_{yy} , and α_{yx} are in fact negative⁴ (for $|z| < 2H$) as suggested by Brandenburg (1998).

4. CONCLUSIONS

The primary goal of our work was to make contact with recent results by BCMR, and to complement their work with a direct measurement of mean-field dynamo effects via the TF method. Given that we have used a very similar numerical method and applied identical parameters (i.e. for model M4), it should not surprise the reader that we can satisfactorily confirm all aspects of the corresponding simulation by BCMR. Minor discrepancies arise with respect to the boundary layers, which may be related to the detailed treatment of the hydrostatic equilibrium there.

⁴ i.e. for $z > 0$, and accordingly positive for $z < 0$

Accordingly, we can confirm their main result, namely that – in the presence of *impenetrable* vertical boundary conditions – one observes a transition from a conductively dominated vertical heat transport to a state that is regulated by convective overturning motions. This transition obviously depends on the value of the applied constant thermal diffusivity κ . Like reported in BCMR, in the $\kappa = 0.004$ case, we observe a flat density profile (even with a slight minimum at the disk midplane), and a “tent”-shaped temperature profile – presumably established by convective heat transport as a result of Rayleigh-Taylor-type instability. This case is also associated with a much increased dynamo activity (by an order of magnitude in the TF coefficients, not shown here), resulting in an overall Maxwell stress that is increased by a factor of three compared to the isothermal reference model. Unlike speculated by BCMR, we however do not think that the enhanced dynamo activity is related to the magnetic boundary conditions. This is despite the fact that such a connection indeed exists for the unstratified case (Käpylä & Korpi 2011), where the different magnetic boundary conditions serve to create an inhomogeneity in an otherwise translationally symmetric system. We rather attribute the different dynamo regime to the overall different hydrodynamic state – which however appears largely influenced by the choice of impenetrable boundary conditions.

A separate set of models (M1-M3) with a more natural condition allowing the gas to flow out of the domain shows much less dramatic effects when going to the low thermal diffusivity regime. Naturally, one arrives at moderately hotter disk interiors along with more spread-out, yet still Gaussian density profiles. Dynamo TF coefficients are somewhat altered in this case, along with a roughly 30% higher turbulent Maxwell stress. Establishing a link (Blackman 2010) between the turbulent transport coefficients in the momentum equation (i.e. the Maxwell and Reynolds stresses) and the induction equation (i.e. the α effect, turbulent diffusion, etc.) will be key to understand magnetized accretion in a quantitative manner, and derive powerful closure models in the spirit of Ogilvie

(2003) or Pessah et al. (2006). A possible direct extension of the existing models with varying amounts of thermal conductivity may be to cross-correlate $\langle \overline{M}_{xy} \rangle$ with e.g. α_{yy} for various values of κ . Such a connection has been suggested by Brandenburg (1998) and been derived in the quasi-linear regime by Rüdiger & Pipin (2000). A complication in this endeavor however arises from the fact that the TF coefficients are likely measured in a magnetically affected, i.e. quenched state.

Given the dramatic effect of open versus closed vertical boundaries demonstrated in this paper, it will be of prime interest to study the connection between the disk and the launching of a magnetically driven wind (Ogilvie 2012), including a possible influence of the wind on the disk dynamo. The amount of recent work (Fromang et al. 2012; Moll 2012; Bai & Stone 2012; Lesur et al. 2013) illustrates the importance of this issue. In terms of the vertical boundaries imposed on the temperature, including a transition into an optically-thin disk corona will be important. Then a radiative boundary condition consistent with black-body radiation can be applied. To conclude, we want to emphasize that, clearly, the presented simulations can only be regarded as a first step towards a realistic treatment of the disk thermodynamics. Ideally, full-blown radiative transfer should be employed, and simulations of radiation dominated accretion disks (Blaes et al. 2011) demonstrate that this has indeed become feasible.

The author acknowledges the anonymous referee for providing a well-informed report and wishes to thank Axel Brandenburg and Gianluigi Bodo for useful comments on an earlier draft of this manuscript. This work used the NIRVANA-III code developed by Udo Ziegler at the Leibniz Institute for Astrophysics (AIP). Computations were performed on resources provided by the Swedish National Infrastructure for Computing (SNIC) at the PDC Centre for High Performance Computing (PDC-HPC).

REFERENCES

- Bai, X.-N., & Stone, J. M. 2012, submitted to ApJ, arXiv:1210.6661
 Balbus, S. A., & Hawley, J. F. 1998, RvMP, 70, 1
 Blackman, E. G. 2010, AN, 331, 101
 Blaes, O., Krolik, J. H., Hirose, S., & Shabaltas, N. 2011, ApJ, 733, 110
 Bodo, G., Cattaneo, F., Ferrari, A., Mignone, A., & Rossi, P. 2011, ApJ, 739, 82
 Bodo, G., Cattaneo, F., Mignone, A., & Rossi, P. 2012, ApJ, 761, 116
 Brandenburg, A. 1998, in Theory of Black Hole Accretion Disks, ed. M. A. Abramowicz, G. Björnsson, & J. E. Pringle, 61–
 —. 2008, AN, 329, 725
 Brandenburg, A., Nordlund, A., Stein, R. F., & Torkelsson, U. 1995a, ApJ, 446, 741
 Brandenburg, A., Nordlund, Å., Stein, R. F., & Torkelsson, U. 1995b, in Lecture Notes in Physics, Berlin Springer Verlag, Vol. 462, Small-Scale Structures in Three-Dimensional Hydrodynamic and Magnetohydrodynamic Turbulence, ed. M. Meneguzzi, A. Pouquet, & P.-L. Sulem, 385
 Brandenburg, A., Rädler, K.-H., Rheinhardt, M., & Subramanian, K. 2008, ApJ, 687, L49
 Brandenburg, A., Sokoloff, D., & Subramanian, K. 2012, Space Sci. Rev., 169, 123
 Davis, S. W., Stone, J. M., & Pessah, M. E. 2010, ApJ, 713, 52
 Fromang, S., Latter, H. N., Lesur, G., & Ogilvie, G. I. 2012, submitted to A&A, arXiv:1210.6664
 Fromang, S., & Papaloizou, J. 2007, A&A, 476, 1113
 Gardiner, T. A., & Stone, J. M. 2005, in AIP Conf. Series, Vol. 784, Magnetic Fields in the Universe, ed. E. M. de Gouveia dal Pino, G. Lugones, & A. Lazarian, 475–488
 Gressel, O. 2010, MNRAS, 405, 41
 Gressel, O., Nelson, R. P., & Turner, N. J. 2011, MNRAS, 415, 3291
 —. 2012, MNRAS, 422, 1140
 Gressel, O., & Ziegler, U. 2007, CoPhC, 176, 652
 Johansen, A., Youdin, A., & Klahr, H. 2009, ApJ, 697, 1269
 Käpylä, P. J., & Korpi, M. J. 2011, MNRAS, 413, 901
 King, A. R., Pringle, J. E., & Livio, M. 2007, MNRAS, 376, 1740
 Kitchatinov, L. L., & Rüdiger, G. 2010, A&A, 513, L1
 Lesur, G., Ferreira, J., & Ogilvie, G. I. 2013, A&A, 550, A61
 Miller, K. A., & Stone, J. M. 2000, ApJ, 534, 398
 Miyoshi, T., & Kusano, K. 2005, JCoPh, 208, 315
 Moll, R. 2012, A&A, 548, A76
 Ogilvie, G. I. 2003, MNRAS, 340, 969
 —. 2012, MNRAS, 423, 1318
 Oishi, J. S., & Mac Low, M.-M. 2011, ApJ, 740, 18
 Pessah, M. E., Chan, C., & Psaltis, D. 2006, PhRevL, 97, 221103
 —. 2007, ApJ, 668, L51
 Piontek, R. A., Gressel, O., & Ziegler, U. 2009, A&A, 499, 633
 Rädler, K. H. 1969, Monats. Dt. Akad. Wiss., Berlin, Volume 11, p. 272–279, 11, 272
 Rheinhardt, M., & Brandenburg, A. 2010, A&A, 520, A28+
 Rüdiger, G., & Pipin, V. V. 2000, A&A, 362, 756
 Schrunner, M., Rädler, K.-H., Schmitt, D., Rheinhardt, M., & Christensen, U. 2005, AN, 326, 245
 Schrunner, M., Rädler, K.-H., Schmitt, D., Rheinhardt, M., & Christensen, U. R. 2007, GAxFD, 101, 81
 Shi, J., Krolik, J. H., & Hirose, S. 2010, ApJ, 708, 1716
 Simon, J. B., Beckwith, K., & Armitage, P. J. 2012, MNRAS, 422, 2685
 Stone, J. M., & Gardiner, T. A. 2010, ApJS, 189, 142
 Vainshtein, S. I., Parker, E. N., & Rosner, R. 1993, ApJ, 404, 773
 Vishniac, E. T. 2009, ApJ, 696, 1021
 Vishniac, E. T., & Brandenburg, A. 1997, ApJ, 475, 263
 Ziegler, U. 2004, JCoPh, 196, 393